REVIEW ARTICLE

.

Bin LI, Jin ZHAO, Min FENG, Ken ONDA

Interferometric two-photon photoemission correlation technique and femtosecond wet-electron dynamics at the TiO₂ (110) surface

Abstract   The femtosecond time-resolved two-photon photoemission (TR-2PP) and the ultra high vacuum (UHV) surface science techniques are integrated to investigate the electronic structures and the interfacial electron transfer dynamics at the atomically ordered adsorbate overlayers on TiO₂ single-crystalline surfaces. Our research into the CH_3OH/TiO_2 system exhibits complex dynamics, providing abundant information with regard to electron transport and solvation processes in the interfacial solvent structures. These represent the fundamentally physical, photochemical, and photocatalytic reactions of protic chemicals covered with metal-oxides.

1   Introduction

Photoemission spectroscopy, especially ultraviolet photo-

Bin LI[1,2] (✉), Jin ZHAO[2], Min FENG[2,3], Ken ONDA[4]

[1] Engineering Center, University of Colorado, Boulder, Colorado 80302, USA
[2] Department of Physics and Astronomy, University of Pittsburgh, Pittsburgh, Pennsylvania 15260, USA
[3] Surface Science Center, University of Pittsburgh, Pittsburgh, Pennsylvania 15260, USA
[4] Department of Chemistry and Materials Science, Tokyo Institute of Technology, O-okayama, Meguro-ku, Tokyo 152-8551, Japan
   E-mail: Bin.Li@colorado.edu, libin1995@yahoo.com

emission spectroscopy (UPS) or X-ray photoemission spectroscopy (XPS), is a well-developed technique widely applied to measure the electronic structures of metals, semiconductors and molecular-solid state interfaces. The key phenomena in photoemission is the photoelectric effect, which was first interpreted in 1905 by Einstein, who postulated that light was composed of discrete quanta of energy $E_L = \hbar\omega_L$. An electron with binding energy I absorbs the quanta light energy, then escapes from the surface, i.e., is photoemitted, with a kinetic energy of [1]

$$E_K = \hbar\omega_L - I \qquad (1)$$

Apparently, the photoemission yield would depend on the energy of incident light, the electronic structure distribution of the investigated solid state materials, the incident angle and the photoelectron emitted angle, as well as the light polarization. Figure 1 shows the photoemission measurement is performed at the incident angle θ and emission from the normal direction of the sample surface.

In Fig. 1, the principle of UPS characterizing valence band electronic structures on a typical metal surface is illustrated. Absorption of a UV photon with energy (usually > 6 eV and < 100 eV) will eject an electron above the vacuum level, detected by an electron energy analyzer. The kinetic energy distribution of the photoelectron, under the one-step model approximation [Eq. (1)], maps the density distribution of the occupied states below the Fermi level (e.g., the states i, ii and their corresponding photoemission density peaks). However, the photoemitted electrons with low kinetic energies barely escaping from the vacuum level are usually associated with multi-step scattering process, appearing as a sharp low energy cutting edge in a UPS spectrum, i.e., secondary electron distribution. Since X-ray has an energy of 100 eV up to keV range, XPS can be employed to investi
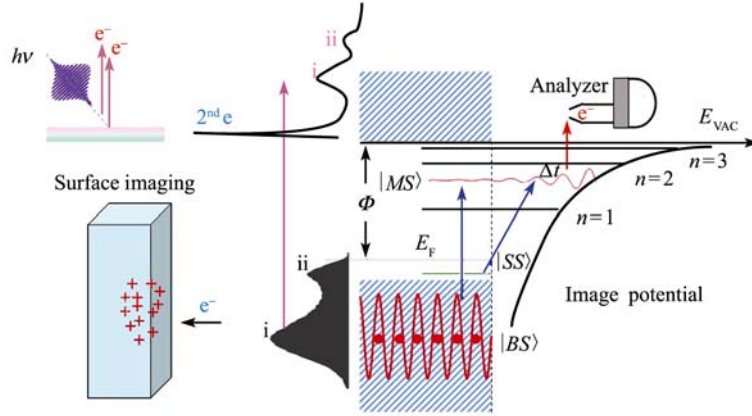
Fig. 1 The schematic represents an electron approaching to a metal surface forming an image potential well and an infinite series of hydrogenic image potential states (n = 1, 2, 3, etc.). A projection bandgap between the valence band and conduction band is illustrated, while the ultra-violet photoemission (UPS) is shown to map the valence density of state (DOS) below the Fermi level (E_F) as the photoelectron distribution above the Vacuum level (E_{VAC}), where Φ indicates the work function. A pump-probe method is illustrated as well to investigate the intermediate state (refer to the text).

gate the core levels' electronic structures, which have much larger binding energies compared to the valence band structures. Many researches on electrons at surfaces involve the study of image-potential states (IPS), associated with unoccupied electronic states distributed above the Fermi level. Whenever an excess electron is approaching from above a metal surface (as in Fig. 1, Left), it induces a negatively polarized charge inside the metal, resulting in an interaction between the electron and the polarized charge density distribution. This leads to the one-dimensional Coulombic potential, i.e., image potential (IP) to support an infinite series of hydrogenic states (n = 1, 2, 3, etc. in Fig. 1, Right), confined by the energy barrier on the surface side and the image potential on the vacuum side. For metal surfaces, the energies of IPS are given by [2, 3]

$$E_n = -\frac{m_e}{32}\left(\frac{e^2}{4\pi\varepsilon_0\hbar}\right)^2 \frac{1}{(n+a)^2} + E_{VAC} \qquad (2)$$

where n represents the principal quantum number and a is the quantum defect parameter. This series converges to E_{VAC}, which is the vacuum energy level for a homogenous surface. The image-potential state electrons usually reside only a few angstroms outside the metal-vacuum interface.

The photo-threshold energy, i.e., the minimal electronic binding energy or work function of metals or semiconductors with clean surfaces, lies typically in the range of 5−7 eV. The work function can be lowered considerably by depositing one monolayer of an alkali metal or chemical molecules. Adsorbate (metals or chemicals) deposition on a metal or oxide surface through physical or chemical interaction will lead to the hybridization of molecular orbitals with the substrate energy states. The overall Hamiltonian can be simplified as [4, 5]

$$\hat{H} = \hat{H}_M + \hat{H}_S + \hat{H}_{ET} \qquad (3)$$

which describes the molecular Hamiltonian, the substrate Hamiltonian and the charge transfer coupling term respectively. The charge transfer term $\hat{H}_{ET}$ corresponds to molecular resonance broadening. At the strong chemisorption case, where the charge transfer energy is larger than the energy bandwidth of the substrate, the adsorbate state would split into bonding and anti-bonding states. These states usually coincidentally correspond to the highest occupied molecular state (HOMO) or lowest unoccupied molecular state (LUMO) respectively. Figure 1 also illustrates the optical excitation process from the bulk states (BS) or surface states (SS) into an unoccupied molecular resonance state (MS). This photo-excitation process is actually associated with an electric dipole transition, or charge transfer process mediated by an MS. The rate of photoexcitation from a SS into a molecular resonance is

$$R_{M \leftarrow SS} = |\langle MS | \boldsymbol{\mu} \cdot \boldsymbol{E} | SS \rangle|^2 \, \delta(E_{MS} - E_{SS} - \hbar\omega) \qquad (4)$$

where $|MS\rangle$ represents the unoccupied molecular states, $|SS\rangle$ or $|BS\rangle$ represents the surface state or bulk eigenstates, $\boldsymbol{E}$ is the electric field vector of the light and $\boldsymbol{\mu}$ is the electric dipole vector. In reality, a photo-excitation process involves the forward charge transfer from multiple initiate states distributed in the bulk or near the surface region $|k\rangle$, and the overall photo-injection rate into a molecular resonance is calculated as

$$
\begin{aligned}
R &= \sum_k R_{M \leftarrow k} \\
&= \sum |\langle MS | \boldsymbol{\mu} \cdot \boldsymbol{E} | k \rangle|^2 \, \delta(E_{MS} - E_k - \hbar\omega_L)
\end{aligned} \qquad (5)
$$

In recent years, the optical pump-probe methodology was developed. The technique involves applying a pump pulse to induce perturbation or modification to a system, and then using a probe pulse arriving at time delays after the pump, to investigate the change and dynamic evolution of the re-searched system. The two-photon photoemission (2PP) spectroscopy [6] representing the basic pump-probe concept was especially established and employed to study electronic structures and dynamics of the unoccupied image potential states and molecular resonance at the surface. In Fig. 1, the 2PP process is principally illustrated as a two-color scheme, where the first photon (red, pump pulse) excites electrons from an occupied state below the Fermi level to an unoccu-pied molecular state (which could be an image state or a virtual intermediate state as well), the second photon (blue, probe pulse) further excites electrons from the unoccupied state to above the vacuum level, and are then detected by the electron energy analyzer. The most significant advantage of the 2PP methodology compared to single photon excitation and photoemission (e.g., UPS, XPS) is that it can provide information not only on the density of state (DOS) of the occupied states below the Fermi level E_F, but also that of the unoccupied states above E_F. Apparently, the latter cannot observe molecular resonance mediated through an unoccu-pied state. Moreover, tuning the arrival times between the pump and probe pulses enables us to record the dynamics of the intermediate state through the change of the 2PP intensi-ties as a function of time-delay. Analyzing the experimental time-resolved 2PP spectra allows us to measure the decay lifetime of the unoccupied states or to retrieve the time scales and mechanisms for the forward or reverse charge transfer processes between the molecular excited states and the metal or oxide substrate. However, the photoexcitation process [Eq. (5)] usually occurs in sub-femtosecond or atto-second time-range, therefore our femtosecond 2PP spec-troscopy mainly reflects the dynamics relevant to electron evolution dynamics instantly after the photoexcita- tion or the reverse charge transfer dynamics of the quasi nonequi-librium molecular excited states.

2   Experimental apparatus

The typical experimental set-up for the time-resolved two-photon photoemission is shown in Fig. 2. The left lower corner shows a schematic representation of the ultrafast Ti: Sapphire oscillator constructed in our laboratory [7]. A commercial continuous wave (CW) solid state Nd:YAG la-ser (Millennia Xs, from Spectra Physics) emitted the 1064 nm laser light, which was frequency-doubled and used as a pump source for the homemade Ti:Sapphire laser. Approxi-mately 6 Watts output power of green light at 532 nm inci-dent at the Brewster's angle is focused with a 50 mm focal lens onto the Ti:Sapphire crystal. The resulting ~800 nm emission is amplified to generate a coherent beam with p-polarization, i.e., the transverse magnetic (TM) mode. Mode-locked fs laser pulses are generated through passive self-phase modulation (SPM), which occurs via the 3rd order nonlinear interaction of a rapidly varying optical field of the laser pulse with the nonlinear intensity-dependent change in the refractive index of an optical material to induce mode-locking for millions of longitudinal modes [8]. The nonlinear index change induces a transient lens effect (Kerr effect) in the gain crystal [9]. Finally, the Ti:Sapphire oscillator delivers an optimal pulse of <15 fs time duration, with a repetition rate of around 90 MHz and an output power of ~650 mW.

The photon energy of ~1.55 eV from the 800 nm laser is frequency doubled through a second harmonic generation (SHG) apparatus employing a type-I β-BBO crystal. A pair of spherical concave reflection mirrors is used to focus the fundamental beam into the crystal to achieve high conver-sion efficiency (~20 %) and deliver a second harmonic light at 120 mW with transverse electric (TE) mode and adjust-able focus. The BBO crystal is set on a gimbal mount, which allows rotation along the tuning axis to maximize the SHG output power or to tune the output wavelength of a broad-band input pulse by changing the phase match angle. The blue light is delivered through a dispersion compensation set-up consisting of a set of mirror-pairs, where each of the mirrors is coated with multi-layer negatively dispersive ma-terials to provide a well-balanced negative group velocity dispersion (GVD) to compensate the positive group velocity dispersion in the optical elements (crystal, lens or beams-plitter) and air. This method turns out to be very efficient and competitive compared with the traditional technique employing two sets of GVD compensation prism-pairs.

Our 2PP technique is based on an updated version of sin-gle color pump-probe methodology, employing a Mach-Zehnder Interferometer (MZI) to represent the time-delay instrument utilized for the interferometric time-resolved two-photon photoemission correlation (I2PC) measurement [6, 7]. The main structure of the MZI is shown in the upper left of Fig. 2. Inside the MZI, two broadband beam splitters designed for 50% reflection of s-polarized 400 nm light at 45° incidence separate and recombine a single pulse into a collinear pulse pair. One of the optical paths is fixed, while the other is scanned with a piezoelectric actuator to generate variable time delay between the pump and probe pulses. The MZI has two light outputs with practically equal intensity. The path for which the dispersion is balanced is used for the
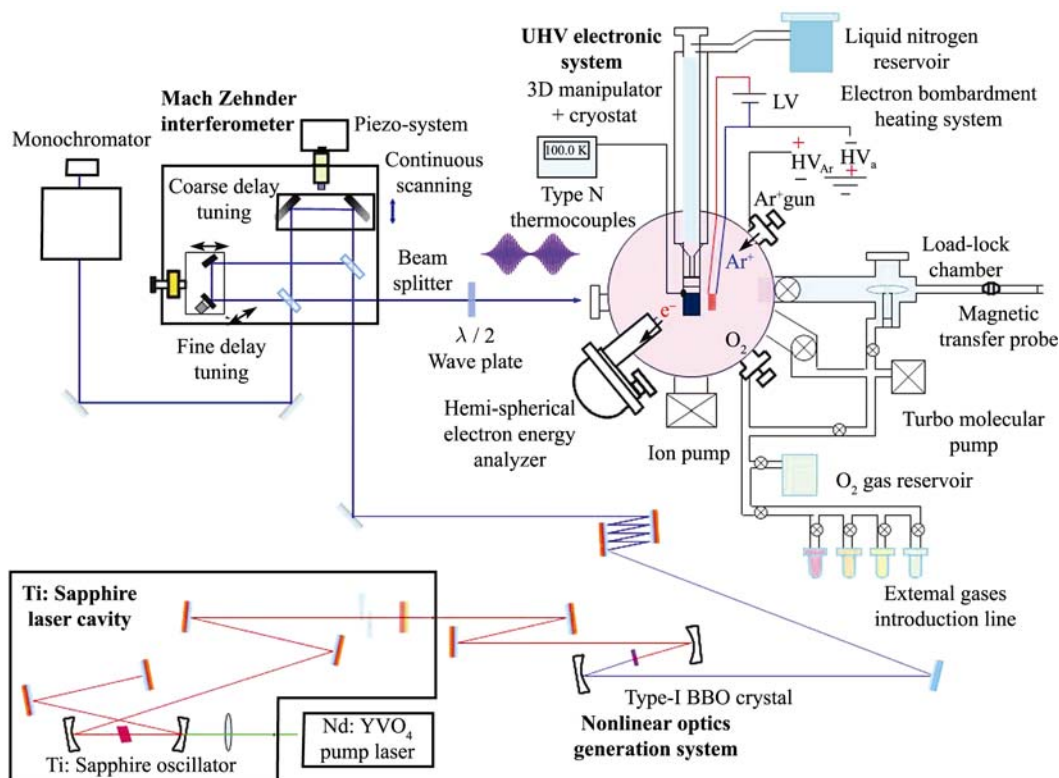
Fig. 2   The experimental apparatus layout, including the overview of the optical system and ultra high vacuum (UHV) electronic system for the time-resolved interferometric two-photon photoemission correlation measurement.

2PP measurements, while the unbalanced part is used for the scan delay calibration, where the monochromator takes the broadband femtosecond light and selects only a narrow band (usually at the wavelength associated with the spectral intensity maximum) that is detected with a photomultiplier. The narrow band selection stretches the femtosecond pulses to the nanosecond time scale. As a result, the pump and probe pulses at the output of the monochromator overlap in space and time throughout the delay scan, and the optical interference between the pulses provide a sinusoidal signal whose period corresponds to an optical cycle of the monitor light of about 1.33 fs. In the meantime, the balanced excitation light passes through a $\lambda/2$ waveplate as an option before entering the ultra high vacuum (UHV) photoemission chamber to switch in-between p- or s-polarization. A differentially pumped CaF_2 lens with a nominal focal length of 200 mm mounted on the UHV chamber focuses the excitation light onto the sample and simultaneously serves as a transparent vacuum seal. The focus size on the sample is estimated to be less than 100 μm.

The time-resolved photoemission measurement is performed in a UHV chamber with a base pressure $\sim 1.0 \times 10^{-10}$ mbar. The sample is mounted at the bottom end of a custom UHV manipulator. The manipulator has capability for 3D

translation and rotation involving a differentially pumped stage. The manipulator is used to position the sample to desired coordinates to perform various surface treatments such as Ar^+ sputtering, e^- irradiation, molecular deposition, and photoemission measurements. The manipulator has a hollow center working as the reservoir of a liquid nitrogen flow cryostat. Sample heating is accomplished through electron bombardment. When applying a high voltage ($HV_e \sim 1$ kV) with respect to the sample transfer plate, the electrons evaporate from a coiled hot tungsten wire passing a filament current of ~ 2 A, are accelerated and hit the backside of the transfer plate. The final sample temperature depends on the magnitude of both the acceleration potential HV_e and the electron emission current. Using the combination of liquid N_2 cooling and the electron bombardment heating, the sample temperature can change from 85 K up to 1000 K. The TiO_2 sample is clamped at its upper and lower edges by two flexible molybdenum springs and mounted onto the front side of the transferable sample plate. An N-type thermocouple, which is made of a nonmagnetic material, is spot welded onto a fixed spring that holds the aforementioned sample plate to measure the sample temperature over a wide range. The UHV system is designed to allow for the transfer and storage of multiple samples. The load-lock chamber in

Fig. 2 is separated from the main chamber by a gas-gate valve and has a rotatable sample holder, which is capable of storing up to 6 samples. The core measurement instrumentation in the UHV apparatus is the hemispherical electron energy analyzer, whose major function is to collect the photoemitted electrons from the sample surface and perform their energy and momentum measurement and analysis. The energy analyzer is equipped with a multi-channel channeltron detector, and can measure the photoemission intensities at 7 discrete energy levels simultaneously. Its optimal energy resolution can be as good as < 20 meV to provide high quality angularly resolved (or momentum) measurement.

Gases to be adsorbed on the surface (e. g., O_2, H_2O or CH_3OH) can be introduced into the chamber by back-refilling through a leak valve. At the bottom division of Fig. 2, an oxygen gas reservoir and several other inlets for introducing chemical vapors into the vacuum system are shown. The oxygen gas is essential for preparing a well-defined stoichiometric TiO_2 surface. The other chemicals, especially CH_3OH, can be deposited onto the prepared TiO_2 surface by back filling. Molecules are chemisorbed onto the sample surface by reducing the sample temperature, typically to 90–100 K, to form stable overlayer structures for photoemission measurements. The oxygen reservoir and the other external gas reservoirs share the same introduction pipe, which is connected to the turbomolecular pump through Swagelok gate valves. When the valves are open, the turbomolecular pump can evacuate the residual gases while the pipes and the manifold are baking; after the manifold is evacuated, new gases can be reloaded and introduced into the chamber.

3   The CH_3OH/TiO_2 surface structures and wet electron state

The electronic structures and dynamic properties of protic solvents, especially H_2O molecules on the metal surface or at the interface, are of fundamental interest and have been investigated extensively. However, compared to metals, much less is known of the electron solvation in molecular overlayers on metal oxides. The acidic/basic sites of the metal-oxide surface can have a strong effect on whether the molecules adsorb associatively or dissociatively, and provide various templates for adsorption of molecular overlayers with different interfacial structures. In this review, we focus on using the CH_3OH molecule to investigate the interfacial electronic structure and charge transfer dynamics on a representative metal oxide, $-TiO_2$ surface.

The electron interaction with hydrous overlayers on rutile

TiO_2(110) surface has been investigated because of interest in the application of TiO_2 nanocolloids to photocatalytic processes (e.g., splitting of H_2O into H_2 and O_2, decomposition of polluted organic molecules, etc.) [10, 11] and TiO_2 based organic photovoltaic solar cell energy conversion [12], where electron transfer efficiency/dynamics plays an essential role. The electronic structure of TiO_2(110) surfaces, which is central to the understanding of these processes, has been studied extensively by photoemission, inverse photoemission, and 2PP spectroscopy. The valence and conduction bands of TiO_2 are derived from the O 2p and Ti 3d states, respectively. For the rutile and anatase polymorphs they are separated by band gaps of 3.05 (Fig. 3) and 3.2 eV. TiO_2 is easily reduced either by the generation of O atom vacancy defects or by chemisorption of electron donors. Upon reduction, a defect energy band forming at ~0.1 eV below the conduction band minimum enhanced the bandgap states significantly.

The interferometric two-photon photoemission correlation (I2PC) measurements were performed on the CH_3OH/TiO_2(110) surface according to the procedures described in our previous publications [13, 14]. 2PP is mediated though a transiently occupied wet electron state, where the excited excess electrons were binded and partially hydrated into the "dangling" H molecular orbitals in the CH_3OH overlayer structures on TiO_2 surface (Fig. 3) [13]. The 2PP spectra, recorded by scanning a hemispherical electron energy analyzer, are dominated by transiently occupied wet electron states. The measurements of electron solvation on CH_3OH/TiO_2(110) surfaces provide much more information of electron solvation in protic solvents on metal oxide surfaces than the measurements at H_2O/TiO_2 surfaces. Similar to H_2O, CH_3OH dissociates at bridging Oxygen (O_b) vacancy defects upon chemisorption on reduced TiO_2(110) surfaces. The dissociative chemisorption incorporates minority $-OH$ and $-OCH_3$ species in the O_b rows. Further chemisorption occurs at the Ti_{5c}^{4+} sites, where according to both experiment and theory, a fraction of the chemisorbed molecules dissociate (deprotonated) to form $-OCH_3$ at the Ti_{5c}^{4+} sites and $-OH$ at the bridging sites within the neighborhood [see the inserted rutile (110) surface structure in Fig. 3]. 2PP spectra for different exposures of CH_3OH on reduced TiO_2 surface are systematically investigated, and the exposure of 1.2 Langmuir of CH_3OH dosage corresponding to ~1 Monolayer (ML) coverage was established for our UHV chamber. At this coverage, the peak of intermediate state at 2.3 eV above the Fermi level attains the maximum intensity (data not shown). Measurements of the resonance dispersion with parallel momentum confirm that the electronic state is localized in the CH_3OH overlayer [15]. Except for the cov-
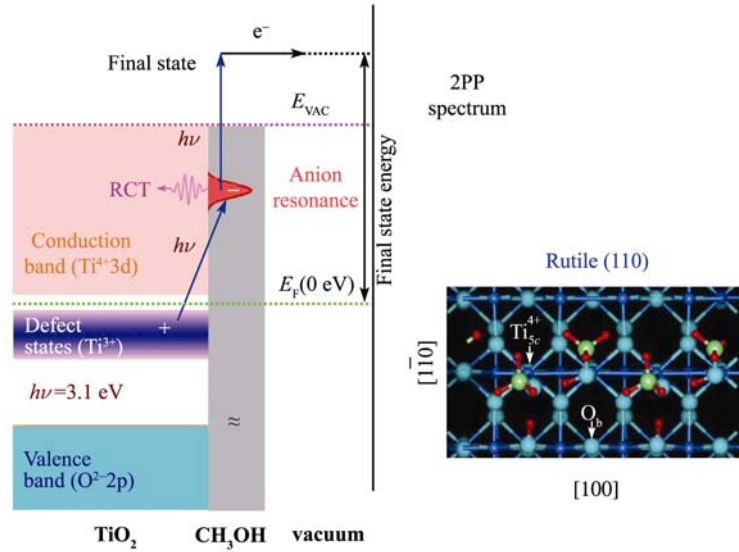
Fig. 3 Schematic diagram for 2PP excitation process at CH₃OH-covered TiO₂ (110) surfaces. The primary process is the charge-transfer excitation from the bandgap states into the CH₃OH overlayer, where the excitation creates a transient anionic state resonance. Further excitation emits electrons form the CH₃OH overlayer above the vacuum level E_{VAC} into the vacuum, the wet-electron state decay through RCT into the CB of TiO₂. The inserted graph shows the Rutile-TiO₂ (110) surface and its coordination. Reprinted from Ref. [7].

erage de- pendent energy shift, considerably higher intensity, and appearance even at stoichiometric surfaces, the CH₃OH induced excited-state resonance peak has similar spectroscopic features as the wet electron resonance on H₂O/TiO₂ surfaces, which indicates a relevant origin. Based on these similarities and electronic structure calculations we attribute the CH₃OH induced peak to partial surface solvation of excess electrons.

4 The interferometric two-photon photoemission technique

The photoexcitation laser pulse is characterized and optimized in advance of performing a time-resolved I2PC measurement by minimizing the net dispersion. The pulse temporal duration and phase information is characterized by a nonlinear interferometric autocorrelation (IAC) diagnostic technique [Fig. 4(a)] [9]. Where a coherent pulse replicas is overlapped in a nonlinear crystal to generate the second harmonic signal, scanning the delay between the two pulses and recording the second harmonic signal provides the autocorrelation trace, which contains the information on the time duration and phase dispersion of the pulse.

This IAC signal is given by [9]

$$G_2(\delta) = A(\delta) + 4\,\mathrm{Re}\{B(\delta) \cdot \mathrm{e}^{\mathrm{i}\omega_l \delta}\} + 2\,\mathrm{Re}\{C(\delta) \cdot \mathrm{e}^{2\mathrm{i}\omega_l \delta}\} \tag{6}$$

The A, B and C terms are the fundamental, the first order

and the second order envelopes (at the time delay δ) respectively, given by the following three equations:

$$\tilde{A}(\delta) = \int_{-\infty}^{\infty} \mathrm{d}t \left\{ \varepsilon_1^4(t-\delta) + \varepsilon_2^4(t) + 4\varepsilon_1^2(t-\delta)\varepsilon_2^2(t) \right\} \tag{7.1}$$

$$\tilde{B}(\delta) = \int_{-\infty}^{\infty} \mathrm{d}t\theta \left\{ \varepsilon_1(t-\delta)\varepsilon_2(t)[\varepsilon_1^2(t-\delta) + \varepsilon_2^2(t)] \right. $$
$$\left. \cdot \mathrm{e}^{\mathrm{i}[\varphi_1(t-\delta)-\varphi_2(t)]} \right\} \tag{7.2}$$

$$\tilde{C}(\delta) = \int_{-\infty}^{\infty} \mathrm{d}t \left\{ \varepsilon_1^2(t-\delta)\varepsilon_2^2(t) \cdot \mathrm{e}^{2\mathrm{i}[\varphi_1(t-\delta)-\varphi_2(t)]} \right\} \tag{7.3}$$

where $\varepsilon_1(t)$ or $\varepsilon_2(t)$, and φ_1 or φ_2 are the electric field intensity and the phase term of the two overlapping light pulses respectively, and ω_l is the central frequency of the laser spectrum. Easily we can see both the first and the second order envelopes, including the phase information, could be used to diagnose the dispersions of the input laser pulse, assuming the pump and probe are identical. A simple derivation shows the peak to background ratio in the IAC signal is 8:1 [Fig.4 (a)]. The phase average signal from IAC is calculated as

$$\langle AC(\delta) \rangle_{pa} = \frac{1}{T\omega} \int_{\delta-\lambda/2c}^{\delta+\lambda/2c} G_2(t)\mathrm{d}t \tag{8}$$

Figure 4(a) shows that a phase averaged IAC signal is characterized by a main Gaussian peak with FWHM 19 fs corresponding to the input laser pulse width of ~13.5 fs and a substructure wing, indicating the uncompensated higher order optical dispersion term.
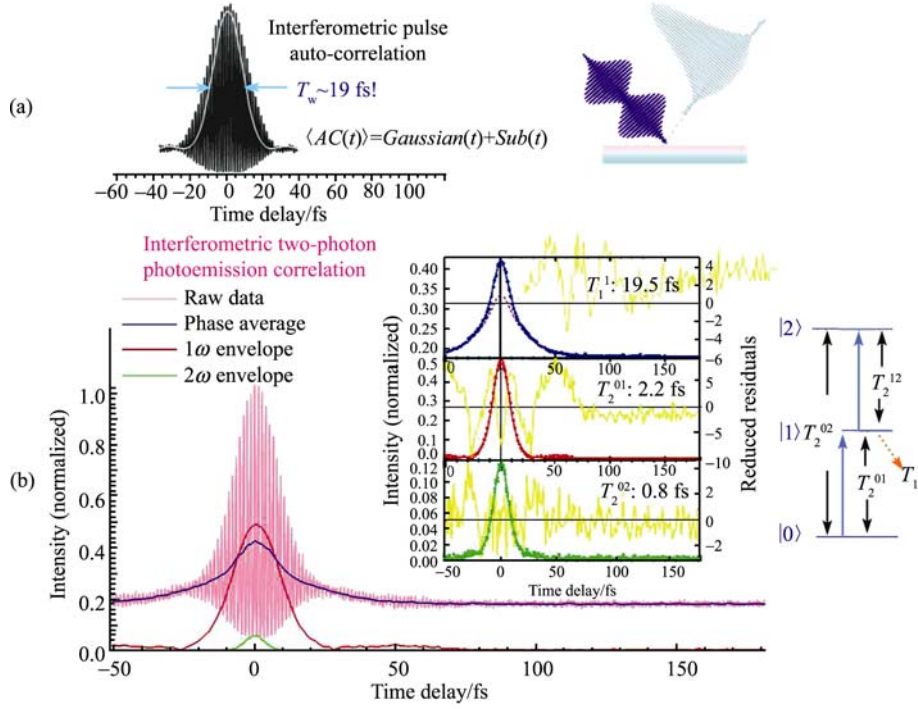
Fig. 4 **(a)** The interferometric autocorrelation signal for a typical Gaussian pulse. **(b)** A typical I2PC signal for adsorbate covered TiO$_2$ surface, and it is decomposed into three components: 0ω, 1ω, 2ω envelopes within a three-energy-level system. Fitting of the envelops provides the coherent polarization and incoherent population decay times.

The interferometric two-photon photoemission correlation (I2PC) measurements are very similar to the nonlinear interferometric autocorrelation signal (IAC). However, they are electronic signals instead of optical signals, containing information on the excess electron population and polarization dynamics as well, which broaden the temporal width [Fig. 4(b)]. The photon pulse incident on the sample surface induces linear or non-linear polarization, which oscillates coherently at the excitation frequency or its higher harmonics. Meanwhile, the photoexcited electron decays incoherently through e-e elastic scattering, or possibly via other charge transfer channels. Coherent interaction with linear or non-linear polarization gives interference at both 1ω and 2ω frequencies; and the incoherent excitation of hot electrons above the Fermi energy level gives a phase independent component.

Therefore the I2PC signal can be decomposed into three different parts: the phase average 0ω, the 1ω envelope, and the 2ω envelope component. All three envelopes can be extracted from the experimental I2PC signal $I(\delta)$ (δ being the same as the time-delay between pump and probe pulses) by Fourier transformation over each optical cycle, which is demonstrated in Fig. 4(b) as [16]

$$I_{2\omega}^{\exp}(\delta) = \frac{4\lambda}{c}$$

$$\cdot\sqrt{\left[\int_{\delta-\lambda/4c}^{\delta+\lambda/4c} I^{\exp}(t)\cos(2\omega_l t)\mathrm{d}t\right]^2 + \left[\int_{\delta-\lambda/4c}^{\delta+\lambda/4c} I^{\exp}(t)\sin(2\omega_l t)\mathrm{d}t\right]^2}$$

$$(9.1)$$

$$I_{1\omega}^{\exp}(\delta) = \frac{2\lambda}{c}$$

$$\cdot\sqrt{\left[\int_{\delta-\lambda/2c}^{\delta+\lambda/2c} I^{\exp}(t)\cos(\omega_l t)\mathrm{d}t\right]^2 + \left[\int_{\delta-\lambda/2c}^{\delta+\lambda/2c} I^{\exp}(t)\sin(\omega_l t)\mathrm{d}t\right]^2}$$

$$(9.2)$$

$$I_{pa}^{\exp}(\delta) = \frac{\lambda}{c}\int_{\delta-\lambda/2c}^{\delta+\lambda/2c} I^{\exp}(t)\mathrm{d}t \qquad (9.3)$$

which correspond to 2ω (green), 1ω (red) and 0ω (blue) curves in Fig. 4(b) respectively. The temporal width and shape of these components are determined both by the energy and phase relaxation time scales of the hot electrons in the sample and obviously by the excitation laser pulse width as well. From the IAC signal [in Eqs. (6) and (7)] for a Gaussian pulse with negligible dispersion, $\varepsilon(t) \propto \exp[-2(t/T_0)^2]$, we have

$$G_2(\delta) = 1 + 2\exp\left[-\left(\frac{\delta}{T_0}\right)^2\right]$$

$$+ 4\exp\left[-\frac{3}{4}\left(\frac{\delta}{T_0}\right)^2\right]\cos(\omega_l\delta)$$

$$+ \exp\left[-\left(\frac{\delta}{T_0}\right)^2\right]\cos(2\omega_l\delta) \tag{10}$$

Therefore, using the FWHM pulse width representation $\tau = 2\sqrt{\ln 2}T_0$, the three decomposed components of an I2PC signal are

$$I_{2\omega} \propto \exp\left[-4\ln 2\left(\frac{\delta}{\tau}\right)^2\right]$$

$$I_{1\omega} \propto \exp\left[-3\ln 2\left(\frac{\delta}{\tau}\right)^2\right]$$

$$I_{0\omega} \propto \exp\left[-4\ln 2\left(\frac{\delta}{\tau}\right)^2\right]$$

Then $I_{2\omega}(\delta)$ gives the coherent dephasing time scale $T_2^{(02)}$ between energy states $|0\rangle$ and $|2\rangle$; the component $I_{1\omega}(\delta)$ contains the dephasing time scale $T_2^{(01)}$ between $|0\rangle$ and $|1\rangle$ states; and the phase averaged component $I_{0\omega}(\delta)$ has contribution from both the coherent polarization decay $T_2^{(01)}$ and the incoherent population decay T_1^1 at the intermediate state $|1\rangle$, as illustrated as an inserted diagram in Fig. 4(b).

The fitting formulas for all three components are thus constructed as the convolution between the coherent or incoherent dynamical decay and the phase-averaged pulse auto-correlation, where single exponential decay kinetics in a regular OBE function is used and τ is the FWHM IAC pulse width introduced previously,

$$I_{2\omega}^{\text{fit}}(\delta) = c_0^{2\omega}\int_{-\infty}^{\infty} e^{-\left|\frac{\delta-t}{T_2^{02}}\right|}e^{-4\ln 2(\frac{t}{\tau})^2}\,dt \tag{11.1}$$

$$I_{1\omega}^{\text{fit}}(\delta) = c_0^{1\omega}\int_{-\infty}^{\infty} e^{-\left|\frac{\delta-t}{T_2^{01}}\right|}e^{-3\ln 2(\frac{t}{\tau})^2}\,dt \tag{11.2}$$

$$I_{pa}^{\text{fit}}(\delta) = c_0^{pa}\left[1 + c_1\int_{-\infty}^{\infty} e^{-\left|\frac{\delta-t}{T_1^1}\right|}e^{-4\ln 2(\frac{t}{\tau})^2}\,dt \right.$$
$$\left. + c_2\int_{-\infty}^{\infty} e^{-\left|\frac{\delta-t}{T_2^{01}}\right|}e^{-3\ln 2(\frac{t}{\tau})^2}\,dt\right] \tag{11.3}$$

Through this fitting algorithm to a specific I2PC signal given in Fig. 4(b), we can determine the coherent dephasing time scales $T_2^{(02)} = 0.8$ fs, $T_2^{(01)} = 2.2$ fs, and under the signal exponential decay approximation, incoherent kinetic decay time scales at the intermediate unoccupied state $T_1^1 = 19.5$ fs. Nessler *et al.* first applied this fitting procedure to the study of hot electron dynamics in a High T_c superconducting material Bi2212 [16] and observed the temperature dependent electron lifetimes; their results also exhibit the inverse square rule predicated by electron-electron scattering mechanism [17, 18].

5   The kinetic scheme for CH₃OH dynamics

Time-resolved measurements and the pre-described I2PC signal decomposition technique are applied to investigate wet-electron dynamics in the CH_3OH overlayer on TiO_2 surface with various amount coverages (from ~0.3 ML up to ~2.0 ML), where one monolayer was characterized as 1.2 Langmuir CH_3OH dosage and the 2PP spectrum has the maximal integrated intensity [15]. Our results indicate that excited state dynamics strongly depends on CH_3OH coverage. In Fig. 5(a) we compare the phase averaged I2PC signals obtained from the method discussed in the previous section at the energy level associated with the 2PP intensity maximum (resonance energy) for each of the measured CH_3OH coverages. Compared with the pulse autocorrelation signal, the normalized I2PC signals have similar central shapes, indicating the coherence decay time <1 fs. The broader and coverage dependent wings indicate much longer and more complex population dynamics. In contrast to the wet- electron feature in an H_2O/TiO_2 system [14], the typical I2PC at the resonance energy for different CH_3OH coverages is significantly different: The decay time of the I2PC increases significantly as CH_3OH coverage increases; at higher CH_3OH coverage, the substructure in the autocorrelation trace due to the nonlinear dispersion is washed out because of the longer electron decay time. However, at and above 1 ML coverage, a distinct new sub-peak feature appears, exhibiting coverage dependent non-exponential decay kinetics [7].

To quantitatively investigate and develop a model to describe the wet-electron dynamics on CH_3OH/TiO_2 surfaces, we systematically performed time-resolved measurements for a spectrum of energies across the methanol resonance induced by various coverages and present the results in three dimensional (3D) contour plots in Fig. 5(b). These plots are constructed from I2PC measurements recorded at 0.1 eV intervals, which are combined to provide a map of 2PP emission intensities (indicated by different colors) at different energies (vertical axis) and pump-probe delays (horizontal axis). These 3D plots in Fig. 5(b) obtained for various CH_3OH coverages show that the CH_3OH induced wet-electron state density spreads over a broad energy range of 0.5–0.7 eV, and that the decay time scales increase with the CH_3OH coverage, from roughly 35 fs at ~0.3 ML to above 200 fs at ~2.0 ML. The 3D plots in Fig. 5(b) are composed of I2PC scans spanning around 20 different energies. The 2PP intensity scale is given by the bar code in the figure. The 3D plot clearly shows that the lifetimes are long (e.g. relative to the clean surface) and coverage dependent; while below the resonance, where the 2PP processes mediated by virtual intermediate states, the I2PC trace widths are laser
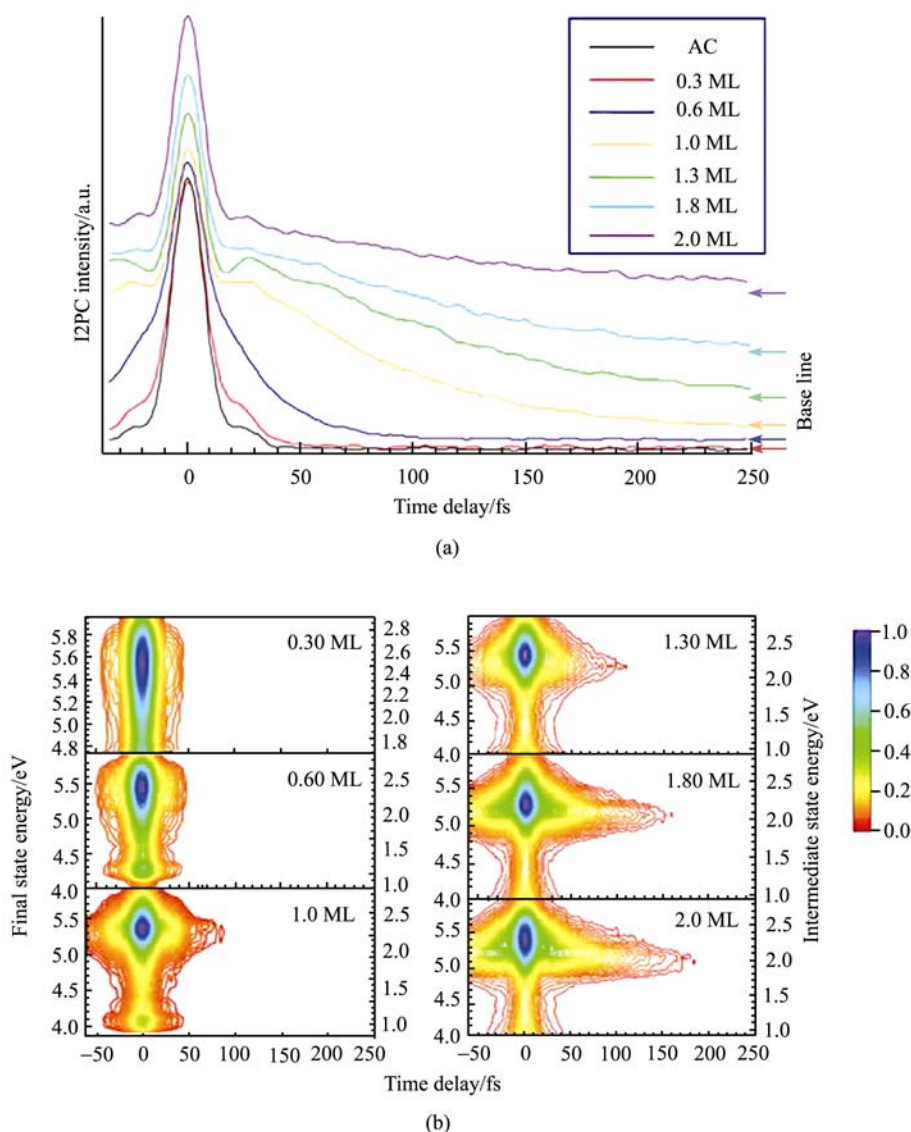
Fig. 5 **(a)** The typical normalized I2PC scans for different coverages of CH_3OH adsorbed TiO_2 surfaces (from 0.3 ML up to 2.0 ML). The arrows at the low-right corner indicate that the appropriate offsets are used. The pulse autocorrelation (AC) trace is given in black as a control signal. **(b)** The 3D contour plots of the 2PP intensity profiles for the different amounts of CH_3OH adsorbed TiO_2 surfaces as a function of pump-probe delay. The left axis indicates the final state energy, and the right axis is the intermediate state energy. The 3D plots are constructed from I2PC measurements taken at 0.1 eV intervals. The bar graph on the right represents the normalized intensity scale where the peak intensity at each coverage is set to 1.0. Reprinted from Ref. [7].

IAC pulse width limited. We will employ such 3D plots to present and analyze electron dynamics in the methanol overlayer structures on the TiO_2 surfaces in the following sections.

Besides remarkable coverage and energy dependence [Fig. 5(a, b)] revealed in the measurement of wet-electron dynamics on the CH_3OH deposited TiO_2 surfaces, we also find that in a certain coverage and energy range the I2PC signals do not obey the single exponential decay kinetics. This is

especially true at the energy levels below the resonance energy for CH_3OH coverages of >1 ML. More detailed investigations and analysis of the CH_3OH/TiO_2 system in Section 6 indicate that the CH_3OH-related electron dynamics include both population and energy relaxation processes, as well as a pronounced deuterium isotope effect. Obviously, this complex kinetics cannot be explained by the standard 3-level scheme involving a single transiently localized intermediate state [Fig. 4(b)] [14]. To simulate the experimental data and

retrieve the time decay constants for the various relevant kinetic processes, we modified the standard Optical Bloch Equation (OBE) model by proposing two close lying intermediate states [Fig. 6(a)]. In the proposed model, the ground states 0 are the occupied bandgap states below the Fermi level, while the final states 2 are the free electron states above the vacuum level as before. The intermediate states 1 and 1* represent the intermediate molecular resonance excited states that are responsible for the observed dynamics [13].

We now consider the population decay of the intermediate energy states following the photo-excitation process. Initially, the photoexcitation transfers electrons from the band gap DOS and mainly populates the higher intermediate state 1. However, the simulation shows the lower energy state 1* could also be mildly populated (< 30 %). After excitation, the population of the higher energy level N_1 partially transfers into the lower energy level N_{1*} through an energy relaxation process with a time scale T_1^{11*}. In parallel with the energy relaxation from $1 \rightarrow 1*$, the population relaxation occurs from both states by the reverse charge transfer (RCT) [7] to the conduction band (CB) of the TiO$_2$ sub-

strate (Fig. 3), similar to the H$_2$O/TiO$_2$ system. The excess electron population decay times in both of these excited states through the aforementioned RCT process are denoted as T_1^1 and T_1^{1*} respectively. In Fig. 6(a), the coherence decay time scales (e.g., T_2^{01}) are indicated as well.

According to the model in Fig. 6(a), a set of differential equations [Eqs. (12.1) and (12.2)] can be used to describe the photoexcited electron population and energy relaxation dynamics at the intermediate states 1 and 1*, where we simplify the notation for the decay parameters in Fig. 6(a) by the notation:

$$T_1^1 \rightarrow \tau_1', \quad T_1^{1*} \rightarrow \tau_{1*}, \quad T_1^{11*} \rightarrow \tau_{11*}$$

The differential equations describing the evolution of 1 and 1* are given by

$$\frac{\mathrm{d}N_1(t)}{\mathrm{d}t} = -\frac{1}{\tau_1'}N_1(t) - \frac{1}{\tau_{11*}}N_1(t) \tag{12.1}$$

$$\frac{\mathrm{d}N_{1*}(t)}{\mathrm{d}t} = -\frac{1}{\tau_{1*}}N_{1*}(t) + \alpha\frac{1}{\tau_{11*}}N_1(t) \tag{12.2}$$
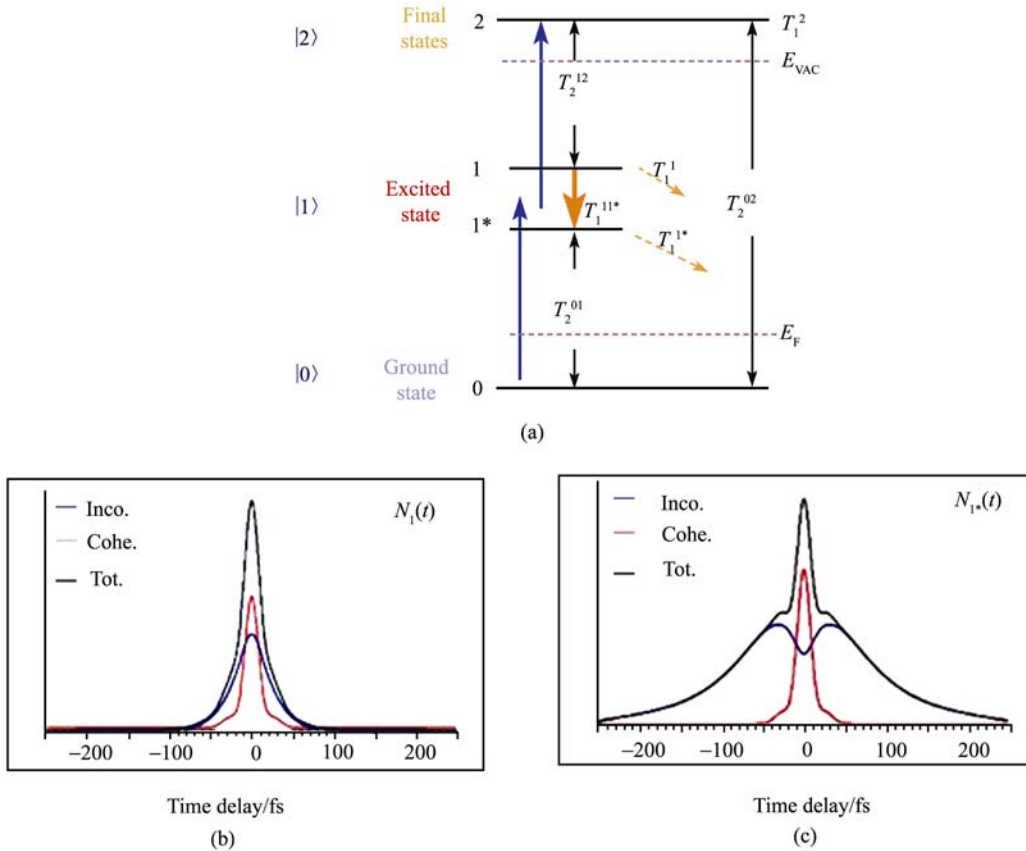

Fig. 6 **(a)** The modified OBE mechanism involving non-exponential decay at the intermediate state [31] used to simulate the observed kinetics, where the ground state 0 is below E_F, the final state 2 is above E_{VAC}, and the intermediate states include two separate energy levels 1 and 1*. **(b)** Decomposition of the coherent/incoherent components of the electron dynamics at the higher intermediate energy level $N_1(t)$, and **(c)** at the lower energy level $N_{1*}(t)$. The fitting parameters are described in the text. Reprinted from Ref. [7].

where the free parameter α is used in the second equation as a filling factor to model a continuum of the intermediate excited states with a two-state model. The population decay rate at the higher energy level N_1 includes the contribution from both the population relaxation from the molecular overlayer through RCT (τ_1') and the energy relaxation to 1* (τ_{11*}) [7, 13]. However, since both processes lead to the decay of state 1, the combined effect can still be simulated by single exponential decay kinetics $1/\tau_1 = 1/\tau_1' + 1/\tau_{11*}$. The total decay time of the primary photoexcited state 1 corresponds to the rise time of the 1* state. The population kinetics of the 1* state includes the energy relaxation from the higher lying 1 state, as well as the exponential decay through both RCT and a significantly slower energy relaxation process probably related to the electron solvation. Since the 1* state decay kinetics again includes both energy and population decay, we can combine these two rates into a single process. Thus, the intermediate state populations 1 and 1* evolve according to:

$$N_1(t) = N_1^0 e^{-\left(\frac{1}{\tau_1'} + \frac{1}{\tau_{11*}}\right)t} = N_1^0 e^{-\frac{1}{\tau_1}t} \tag{13.1}$$

and

$$N_{1*}(t) = N_{1*}^0 e^{-\frac{1}{\tau_{1*}}t} + \alpha \frac{N_1^0}{\tau_{11*}} \frac{\tau_1 \tau_{1*}}{\tau_1 - \tau_{1*}} (e^{-\frac{1}{\tau_1}t} - e^{-\frac{1}{\tau_{1*}}t}) \tag{13.2}$$

where N_1^0 and N_{1*}^0 are the initial amplitudes, and τ_1 and τ_{1*} are electron energy and population decay time scales for N_1 and N_{1*} respectively. For N_{1*}, the extent of the rising amplitude and the time that the population reaches its peak are determined both by the parameter α and the energy relaxation time scale τ_{11*}. We will employ this model to analyze methanol dynamics and discuss the physical meaning of the various time scales in Eqs. (13.1) and (13.2) in the next section.

To simulate the population dynamics at the 1 and 1* intermediate states [refer to Fig. 6(b), (c)], we analyze the phase-averaged experimental I2PC scans employing the scheme in Section 4: The coherent component (mainly involving the decoherence time scale between ground state and intermediate state, i.e., T_2^{01}) of the 2PP process is added to the incoherent components described by Eqs. (13.1) and (13.2), and the sums are convoluted with the pulse autocorrelation,

$$\text{I2PC}_{pa}^{\text{Sim}}(\Delta t) = c_0$$
$$+ c_1 \begin{Bmatrix} N_1(t) \\ N_{1*}(t) \end{Bmatrix} \otimes \langle AC(\Delta t) \rangle + c_2 \exp\left(-\frac{t}{T_2^{01}}\right) \otimes \langle AC(\Delta t) \rangle$$
$$\tag{14}$$

The parameters c_1 and c_2 are variable coefficients used to

obtain the correct amplitudes of the coherent and incoherent components of the I2PC signals for the N_1 or N_{1*} dynamic, and c_0 gives the baseline. The ratio of the coherent and the incoherent contribution is determined by photo-excitation and electron decay kinetics in each specific system [19].

6 Isotope effect and proton-coupled electron transfer mechanism

To understand the electron dynamics in different CH_3OH overlayer structures unveiled in the previous sections more precisely, we perform I2PC measurements for three comparable coverages of CH_3OH (left-side in Fig. 7) and CH_3OD (right-side) from <1 ML to ~2 ML, and present the 3D plots of 2PP intensity decay profiles as a function of both energy and pump-probe delay. The motivation for performing I2PC measurements on the deuterated molecule is the well-documented $\sqrt{2}$ slower inertial component of electron solvation in D_2O compared with H_2O. The observation of such an isotope effect would provide additional information on the molecular vibrational response to the injection of excess electrons.

In Fig. 7, each 3D plot is constructed from the I2PC intensities at 14 different energies encompassing the methanol resonance. Horizontal cuts through the 3D plots [e.g., Fig. 7(B)] give the original interferometric two-photon correlation (I2PC) scans [Fig. 7(B$_i$)]. By simulating the I2PC scans based on the above model [Eq. 14] for both the H and D substituted molecules, we can present and compare the extracted time constants for related processes in Fig. 8(a). As can be seen in Fig. 7, the proposed model provides a good representation of the observed dynamics. The deduced decay parameters from the simulation show the following trends: (1) at low coverages ($\leqslant$1 ML), methanol resonance decays within 30 fs independent of energy or isotopic substitution; (2) above 1 ML, coverage includes both the excited state population and its energy decay with fast and slow components; (3) only the slow decay components depend strongly on the methanol coverage; and (4) most significantly, the slow population decay shows a pronounced deuterium isotope effect.

The results presented in Fig. 7 show the characteristic time scales for the fast and slow decay components for the protonated and deuterated molecules. Based on the time scales, the nature of the decay process, and the isotope effect, we attribute the physical and chemical interpretation to the observed electron dynamics in the methanol overlayer. As we discussed previously, the dynamics of electrons described by $N_1(t)$ involve both the population decay and energy
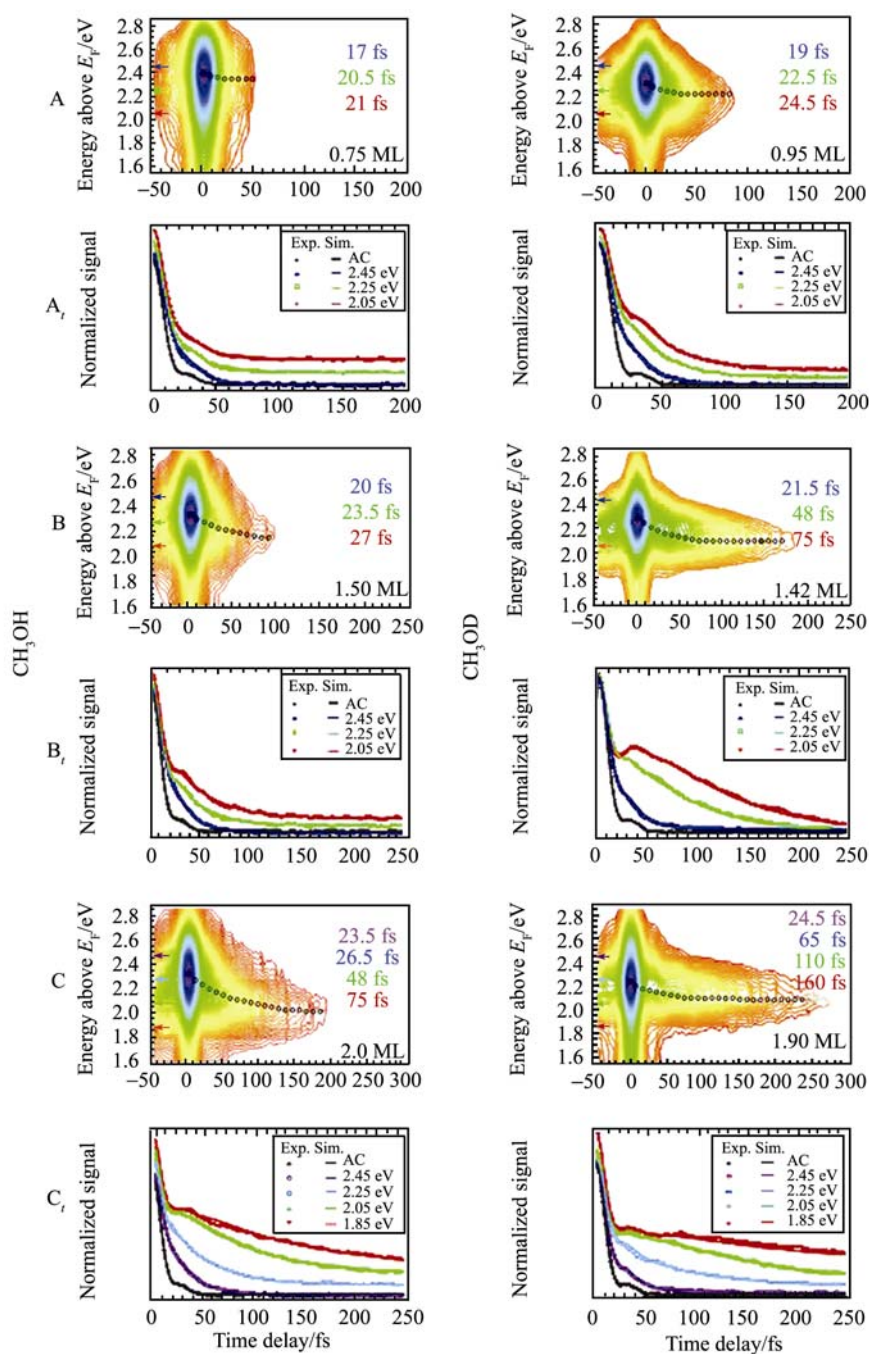
Fig. 7 (**A**, **B**, and **C**) The top panels show three-dimensional 3D plots of the energy and population dynamics of the wet electron state on CH₃OH and CH₃OD/TiO₂(110) surfaces for <1−2 ML coverages that show the strong dependence of the wet electron state dynamics on the methanol coverage and D isotope substitution. The 3D plots are constructed from phase-averaged I2PC measurements taken at 0.1 eV intervals. The black circles indicate the change in the resonance maximum with time. (**A**$_t$, **B**$_t$, and **C**$_t$) The bottom panels show the original I2PC used to construct the 3D plots at several characteristic energies indicated by the color-coded arrows in (**A**) to (**C**) and their simulation (*solid lines*) according to the model described in Fig. 6 and the text. Reprinted from Ref. [13].

relaxation to the 1* state. The population decay probably occurs by RCT into the conduction band of TiO₂ similar to H₂O/TiO₂. Simultaneously, N_1 decays in energy by ~0.1 eV to a quasi-stationary state 1* on a time constant τ_{11^*} within 30 −

40 fs. According to Fig. 8(a), the time scale for the decay of N_1 is essentially isotope independent, since the slope for τ_1 is 1.1. Because the photoexcitation involves the charge redistribution from the $Ti_{5c}^{+4-\delta}$ sites (correspon-ding to the

bandgap states distributed over the defects) to the methanol overlayer, the fast energy relaxation process (30 – 40 fs) which barely depends on the interfacial structures probably involves polaron formation. The photoinduced charge redistribution prompts the inertial screening response of the lattice ions. This assignment is consistent with the energy and time scales for polaron formation through the excitation of ~24 THz longitudinal optical phonons in TiO₂ crystals [20]. Substantial electron-lattice correlation in TiO₂ is also evident in both the electronic structure of bridging oxygen atom vacancy defects and the transient photoconductivity of TiO₂ [20, 11]. This inertial dielectric response stabilizes N_{1*} with respect to the population decay by RCT.

The observed trends for the evolution of the 1* state given by $N_{1*}(t)$ can be used to interpret the photoelectron dynamics below the CH₃OH resonance energy [e.g., 2.05 eV, Fig. 7 (B_t)] for the 1* state. A rise time τ_1 and a slower RCT population decay kinetics τ_{1*} with coverage and isotope dependence characterize the I2PC signal at this energy. The energies corresponding to the 2PP intensities maximum relaxes first because of the fast polaron formation in 30–40 fs, and for longer delays due to the RCT process on account of a much slower process with time scale of > 200 fs [e.g., Fig. 7 (C)]. Based on similar 2PP measurements for CH₃OH/Ag(111), we attribute this energy relaxation process to the injected charge solvated by CH₃OH molecules with a time

constant τ_{sol} [22]. Thus, the total decay rate of $N_{1*}(t)$ can be described as a joint effect including a reverse charge transfer process (RCT) and injected charge solvation in the CH₃OH overlayer, $1/\tau_{1*} = 1/\tau_{RCT} + 1/\tau_{sol}$.

In contrast to decay of the primary photoexcited state 1, the dynamics described by $N_{1*}(t)$ exhibits a strong deuterium isotope effect, according to the slope of 2.2 ± 0.05 reported in Fig. 8(a). Since solvation in liquid methanol is isotope independent, the source of the observed isotope effect lies most likely in RCT dynamics. Isotope substitution can affect rates of kinetic processes through different mechanisms [13], which may be differentiated through the magnitude of the observed ratio of kinetic parameters. For example, an isotope effect of $\sqrt{m_D/m_H}$ ~1.4 that was observed in the inertial component of electron hydration in liquid H₂O [23] has been attributed to the inertial response of the solvent molecules involving molecular liberation. The substantially larger isotope effect on τ_{1*} of 2.2 is significantly larger than the reduced mass ratio for any conceivable kinetic process involving the motion of a single proton or proton containing species such as vibration or liberation. The larger ratio, therefore, either implies that the kinetic process involves the motion of multiple protons or the tunneling motion of protons where the reduced mass effect enters in an exponent [13].

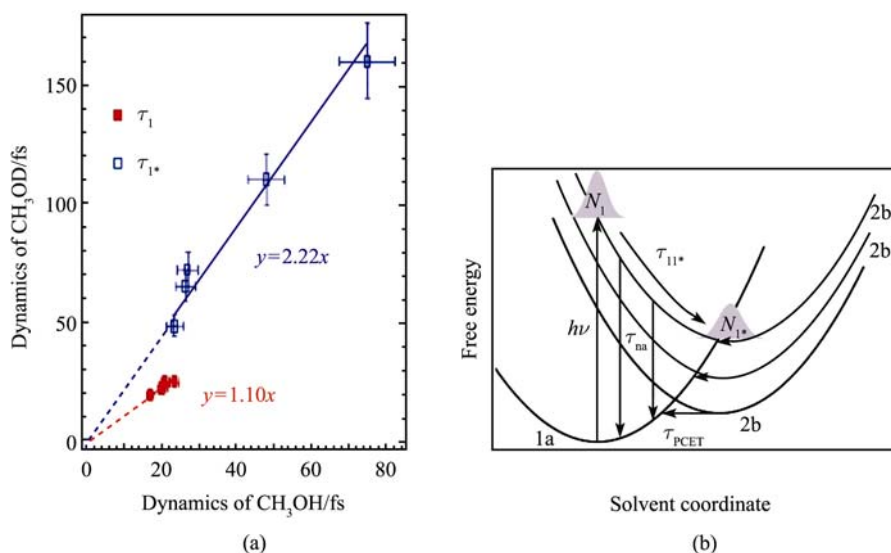The reverse charge transfer dynamics associated with the

Fig. 8 **(a)** The τ_1 and τ_{1*} lifetimes determined for comparable coverage and observation energy for the CH₃OH/TiO₂(110) (abscissa) and CH₃OD/TiO₂(110) (ordinate) surfaces. **(b)** Schematic free energy surfaces for the proton-coupled electron transfer (PCET) plotted against a generalized solvent coordinate. The solid lines represent surfaces for an electron and a proton before (1a) or after (2b) photoinduced transfer; the dotted line (2b′ and 2b″) represent manifold 2b surfaces with different degrees of proton vibrational equilibrium ground state structure (N_1 state) evolve through the inertial dielectric response toward the 2b manifold minima (N_{1*} state). The nonadiabatic electronic decay (*down arrows*) most likely occurs before crossing of the 1a manifold with the 2b manifold. The PCET is the most probable at surface crossing between the 1a and 2b manifolds (*horizontal arrows*). Reprinted from Ref. [13].

N_{1*} population relaxation, which exhibits a significant isotope effect, cannot be explained by a purely electronic process (e.g., inelastic electron scattering). Rather, they are indicative of a correlated electron transfer process that is mediated by the motion of protons or H atoms, i.e., proton-coupled electron transfer (PCET), which is well documented in homogeneous photocatalysis [24, 25]. However, our results first show evidence for such dynamics for molecular overlayers on solid surfaces. Based on this understanding, we describe the total decay rate of $N_{1*}(t)$ with a modified expression, $1/\tau_{1*} = 1/\tau_{PCET} + 1/\tau_{sol}$.

Photoinduced electron transfer under highly nonequilibrium conditions, such as that in the dye sensitized charge injection or the wet electron population decay into TiO$_2$, cannot be described by quasi-equilibrium models such as the Marcus-Jortner theory [26–28]. However, in Fig. 8(b) we draw on the formalism of the Marcus-Jortner theory to propose a scenario for how the inertial structural changes are associated with the dielectric response of the interface control of wet electron dynamics.

The free energy surfaces for the proton and electron transfer are plotted in Fig. 8(b) against a generalized solvent coordinate representing the multi-dimensional dielectric response of the interface to both the electron and proton displacements [29]. Photoexcitation occurs "vertically", i.e., faster than the proton or solvent response shown in Fig. 8(b), from the donor surface 1a (electron at the $Ti_{5c}^{+4-\delta}$ sites and proton at its ground state geometry) to a manifold of acceptor surfaces 2b, 2b$'$, 2b$''$, etc. This manifold represents the excited state where an electron is in the CH$_3$OH overlayer and a proton is displaced with respect to the ground state, with different degrees of excitation of an internal proton vibration. At excitation, a proton in the excited state is strongly displaced along these internal coordinates, and the optical transition terminates on a distribution of vibrationally excited free-energy surfaces. The wave packet created on the 2b manifold evolves toward the surface minimum through the inertial dielectric response. In competition with the dielectric relaxation, the excited state population decays by non-adiabatic processes, which change the state occupation (vertical transitions), and by PCET processes, which exchange the proton and electron between the donor and acceptor states (horizontal transitions) [26]. Exothermic non-adiabatic transitions occur before the wave packet propagates to crossings of the 1a manifold with the 2b manifold. By contrast, PCET is most probable at crossings between 1a and 2b manifolds, where the activation energy (solvent reorganization) is minimum. As the excited state evolves toward the equilibrium structure of a wet electron state, the transition from non-adiabatic to PCET-dominated population decay is re-

vealed by the emergence of the deuterium isotope effect. DFT calculations of the molecular and electronic structure of CH$_3$OH/TiO$_2$ were performed by Zhao *et al.* to provide complementary information with regard to this PCET algorithm; the excited state electronic structure calculation especially provides insight into the PCET, which accounts for the D(H) isotope effect observed at >1 ML coverage [30]. More over, we extend our research into the CH$_3$OH overlayer structures of >3 ML coverage, the wet-electron dynamics displays a much longer decay time-scale, associated with the diffusive electron solvation process lasting up into the pico-second time range preliminarily extrapolated from the afore- discussed PCET mechanism, which will be discussed in detail in our future publication.

7 Conclusion

A wet-electron excited state on a CH$_3$OH/TiO$_2$ surface is discovered and systematically investigated by means of a time-resolved interferometric two-photon photoemission technique (I2PC). Experimental apparatus used in our measurements, including both the ultra-fast pump-probe optical system and UHV electronic devices, are extensively described. This CH$_3$OH induced wet-electron state displays a broadband resonance feature with energy of 2.3 eV above the Fermi level and exhibits complex dynamics that is strongly coverage dependent. Especially at the coverage above one monolayer, the dynamics displays both the population decay and energy relaxation processes, including both fast and slow decay components and a deuterium isotope effect. A kinetic scheme based on the traditional OBE mechanism is developed to simulate the electron kinetics in the CH$_3$OH/TiO$_2$ structure, indicating that the wet-electrons decay through a reverse charge transfer process (RCT) mediated by the correlated motion of H atoms and electrons at the interface. Although such a proton-coupled electron transfer process (PCET) is known in homogeneous electron transfers, this is the first example of such dynamics observed at a molecule/metal-oxide interface. The 2D electron diffusive solvation dynamics is preliminarily discussed.

The "wet-electron" or partially hydrated electron states we observed on the H$_2$O or CH$_3$OH/TiO$_2$ surfaces represent the lowest energy pathway for the non-adiabatic electron transfer. The energy level (2.3–2.5 eV) is associated with the minimum energy that photons must deliver to transport electrons through the interface into the molecular overlayer. Such electrons can drive photochemical or photocatalytic reactions of molecules in the chemisorbed overlayer. Our research is also relevant to the photosensitized charge injec-

tion for the dye-molecules/TiO_2 system, where the wet electron state can present a similarly low energy pathway for transport into the conduction band of TiO_2. Furthermore, similar wet electron states are likely to exist on all protic solvent-covered metal oxide surfaces. Their participation in chemical and physical processes in UHV or under atmospheric conditions can be investigated by methods described within this article.

References

1. A. Einstein, Ann. Phys. (Leipzig), 1905, 17: 132
2. N. Memmel, Surf. Sci. Rep., 1998, 32: 91
3. N. V. Smith, Phys. Rev. B, 1985, 32: 3549
4. C. D. Lindstorm and X. Y. Zhu, Chem. Rev., 2006, 106: 4281
5. M. Galperin and A. Nitzan, Phys. Rev. Lett., 2005, 95: 206802
6. H. Petek and S. Ogawa, Prog. Surf. Sci.,1997, 56: 239
7. B. Li, Ph. D Thesis, University of Pittsburgh, 2006
8. A. Yariv, Quantum Electronics, John Wiley & Sons, 1989
9. J. C. Diels and W. Rudolph, Ultrashort Laser Pulse Phenomena, Academic Press, 1995
10. A. L. Linsebigler, G. Lu, and J. T. Yates, Chem. Rev.,1995, 95: 735
11. P. V. Kamat, Chem. Rev., 1993, 93: 267
12. M. Grätzel, Nature, 2001, 414: 338
13. B. Li, J. Zhao, and K. Onda, et al., Science, 2006, 311: 1436
14. K. Onda, B. Li, J. Zhao, et al., Science, 2005, 308: 1154
15. K. Onda, B. Li, J. Zhao, et al., Surf. Sci., 2005, 593: 32
16. W. Nessler, S. Ogawa, H. Nagano, et al., J. Elect. Spect. Rel. Phen., 1998, 88−91: 495
17. H. Petek, A. P. Heberle, W. Nessler, et al., Phys. Rev. Lett., 1997, 79: 4649
18. S. Ogawa, H. Nagano, and H. Petek, Phys. Rev. Lett., 1997, 78: 1339
19. B. Saleh and M. C. Teich, Fundamentals of Photonics, New York: John Wiley & Sons, INC, 1991
20. E. Hendry, F. Wang, J. Shan, et al., Phys. Rev. B, 2004, 69: 081101
21. T. Minato, J. Zhao, Y. Sainoo, et al., Phys. Rev. Lett., submitted
22. S. H. Liu, J. Phys. Chem. B, 2002, 106: 12908
23. M. S. Pshenichnikov, A. Baltuska, and D. A. Wiersma, Chem. Phys. Lett., 2004, 389: 171
24. S. Hammers-Schiffer, Acc. Chem. Res., 2001, 34: 273
25. R. I. Cukier and D. G. Nocera, Annu. Rev. Phys. Chem., 1998, 49: 337
26. W. Stier and O. V. Prezhdo, J. Phys. Chem. B, 2002, 106: 8047
27. H. Tributsch and L. Pohlmann, Science, 1998, 279: 1891
28. L. G. C. Rego and V. S. Batista, Am J. Chem. Soc., 2003, 125: 7989
29. H. Decornez and S. Hammes-Schiffer, J. Phys. Chem. A, 2000, 104: 9370
30. J. Zhao, B. Li, K. Onda, et al., Chem. Rev., 2006, 106: 4402
31. M. J. Weida, S. Ogawa, H. Nagano, et al., J. Opt. Soc. Am. B, 2000, 17: 1443